Multitip scanning gate microscopy for ballistic transport studies in systems with a two-dimensional electron gas

K. Kolasiński,[1] B. Szafran,[1] and B. Hackens[2]

[1]*AGH University of Science and Technology, Faculty of Physics and Applied Computer Science, al. Mickiewicza 30, 30-059 Kraków, Poland*

[2]*Université Catholique de Louvain (UCL), IMCN/NAPS, 2 Chemin du Cyclotron, 1348 Louvain-la-Neuve, Belgium*

(Received 5 March 2015; revised manuscript received 5 May 2015; published 26 May 2015)

We consider conductance mapping of systems based on the two-dimensional electron gas with scanning gate microscopy using two or more tips of an atomic force microscope. The paper contains the results of numerical simulations for a model tip potential. In addition, a few procedures are proposed for the extraction and manipulation of ballistic transport properties. In particular, we demonstrate that the multitip techniques can be used to obtain a readout of the Fermi wavelength, to detect potential defects, to filter specific transverse modes, and to tune the system into resonant conditions under which a stable map of the local density of states can be extracted from conductance maps using a third tip.

DOI: 10.1103/PhysRevB.91.205314 PACS number(s): 73.23.Hk, 73.63.Rt, 85.35.Be

I. INTRODUCTION

Conductance (G) of open systems with the two-dimensional electron gas (2DEG) in semiconductor heterostructures at low temperatures is determined by scattering of the Fermi level electrons. Using the scanning gate microscopy (SGM) technique [1], one probes the properties of the electron transport in mesoscopic devices by variation of the potential landscape for the Fermi level electrons with the charged tip of the atomic force microscope (AFM) moving above the surface of the sample. The potential of the charge at the tip is screened by the two-dimensional electron gas [2], which produces a short-range form of the effective tip potential for the Fermi level electrons. The SGM technique was widely used in studies of ballistic electron transport, in particular to visualize the electron trajectories as deflected by an external magnetic field [3], electron branching of the Coulomb flow [4,5], including evidence of the quantum Braess paradox [6], formation of a quantum ring potential with a controlled number of modes in each arm [7], investigation of electron backscattering with quantum point contacts [4,5,8], formation of Coulomb islands [9], and mapping the local density of states (LDOS) [10,11]. In addition to the studies of ballistic flow, the tip potential was also used for studies of the charge flow in conditions of the Coulomb blockade in quantum dots [12]. The role of the tip is then to tune the chemical potential of the confined electron system into the transport window defined by the Fermi energies of the source and drain electrodes [12].

In this paper, we consider possible applications of the SGM technique for studies of ballistic transport using two or more tips instead of a single one. We show that the double-tip system can be used for (i) measuring the Fermi wavelength, (ii) mapping the potential defects in the channel, (iii) mode filtering, (iv) detection of localized resonances in an experimental implementation of a stabilization method, and (v) tuning the system to resonant conditions when the LDOS can be read out with a third tip.

Usage of several probes was implemented a few years ago for scanning tunneling microscopy (STM) studies of the sample surface. A version of the STM technique using several independent tips was used in particular to perform four-point measurements [13,14] for determination of the surface properties. Multiple probe experiments have already been performed on nanowires, in scanning tunneling microscopy (STM) mode [14–16], with spacing between the probes controlled down to $\sim$30 nm. In principle, the spacing is only limited by the size of the tip apex (probes with a tip apex as low as $\sim$1 nm are available). In the case of multiple probe scanning gate microscopy experiments, the probe positioning should not be more difficult than in STM mode, and the probe spacing discussed below in this work is within experimental reach with current technological tools.

II. MODEL

We consider ballistic transport at the Fermi level electrons in systems based on a two-dimensional electron gas (2DEG). We neglect the electron-electron interactions and we use the effective-mass Hamiltonian of the form

$$\left\{-\frac{\hbar^2}{2m_{\rm eff}}\nabla^2 + V_{\rm ext}(x,y)\right\}\psi(x,y) = E_{\rm F}\psi(x,y), \qquad (1)$$

where $m_{\rm eff} = 0.067m_0$ is the effective mass of GaAs, $E_{\rm F}$ is the Fermi level energy, and $V_{\rm ext}$ contains all external sources of the electrostatic potential (e.g., potential of the tips $V_{\rm tip}$). The potential of the tip is one of the most critical aspect to control in SGM. The experimental studies of the tip potential for the systems based on 2DEG indicate the Lorentz form of the potential [17], which results from the screening of the Coulomb charge at the tip by the electron gas [2]. The full width at half-maximum of the tip potential turns out to be of the order of tip-2DEG distance [18], and it is independent of the charge at the tip or the density of the 2DEG (see Fig. 6 of Ref. [18]), which only influence the height of the tip potential. Accordingly, we assume that the potential of the tip is given by the short-range Lorentzian potential of amplitude $U_{\rm tip}$ and width $w_{\rm tip}$,

$$V_{\rm tip}(x,y) = \frac{U_{\rm tip}}{1 + [(x-x_{\rm tip})^2 + (y-y_{\rm tip})^2]/w_{\rm tip}^2}. \qquad (2)$$

The Lorentzian form of the potential was also used for previous modeling [11], along the Gaussian [3,19] tip

potential profile. For modeling the scanning gate microscopy of quantum wires above the highly doped substrate, a Coulomb potential with the image charge potential was also used [20]. All the model potentials [3,11,19,20] are smooth and short-range, so qualitatively the simulated conductance maps are quite similar.

In the following, we assume that all the tip potentials have the same width and amplitude and that the distance between them can be changed. The experiments that provide quantitative information on the form of potential use the Coulomb resonances measured on a quantum dot in the Coulomb blockade regime [17]. One can therefore imagine selecting two probes with identical tip potential through similar experiments with quantum dots before starting the multiple probe SGM experiments discussed below.

The shape of the discussed devices—tailored from the sample containing a two-dimensional electron gas—is described by hard-wall boundary conditions.

To solve the scattering problem, we use a finite-difference implementation of the transparent boundary method (TBM) [21–23]. For the boundary conditions in the input lead, we use the standard approach with the wave function given by superposition of incoming and outgoing (reflected) transverse modes,

$$\psi_{\text{input}}(x,y) = \sum_{k=1}^{M_{\text{input}}} \left\{ a_k e^{ikx} \chi_k^{\text{input}}(y) + r_k e^{-ikx} \chi_{-k}^{\text{input}}(y) \right\}, \tag{3}$$

where M_{input} is the number of current propagating transverse modes χ_k^{input} in the input lead, and a_k and r_k are the incoming and reflection amplitudes. For the output lead, we assume that the wave function is given by the formula

$$\psi_{\text{output}}(x,y) = \sum_{k=1}^{M_{\text{output}}} t_k e^{ikx} \chi_k^{\text{output}}(y), \tag{4}$$

where M_{output} is the number of transverse modes χ_k^{output} in the output lead and t_k is the outgoing amplitude. The transverse modes were calculated with the method presented in Ref. [24]. Matching the boundary conditions (3) and (4) with the wave function calculated inside the device, one finds the solution for the scattering problem. After solving Eq. (1) (for details, see [23]) for each incoming mode i, the conductance of the system is calculated from the transmission probability T_i using the zero-temperature Landauer formalism

$$G = G_0 \sum_{i=1}^{M_{\text{input}}} T_i,$$

with $G_0 = \frac{2e^2}{h}$.

In all the cases considered below, we assume that both leads have the same width equal to the width of the channel, thus $M \equiv M_{\text{input}} = M_{\text{output}}$. We choose the discretization grid $\Delta x = \Delta y = 4$ nm. In further discussion, we will refer to the local density of states, which is defined as the sum of electron densities incoming from the left and right lead [2].

The TBM is very similar to the wave-function matching method [24], which is based on the scattering matrix and the wave-function approach. Actually, our method is also similar to the one implemented in the KWANT package [25]. The procedure for finding the wave function inside the device is exactly the same (see Sec. 2.2 of Ref. [25]). To solve the transport problem, one has to find eigenmodes of each contact, incorporate them into the Hamiltonian (1) by using proper boundary conditions [Eqs. (3) and (4)], and then solve the system of linear equations with a huge but sparse Hamiltonian matrix. The computational time needed to solve the problem depends on the solver used. We use the superLU library [26], which performs fast LU decomposition designed for sparse matrices. We find that for a computational box of $L \times L$ mesh points, the computational time scales as $O(L^3)$ compared to $O(L^4)$ for the recursive Green function (RGF) technique. Nevertheless, the memory usage is indeed larger for TBM: $O(L^2 \log L)$ versus $O(L^2)$ for the RGF [25].

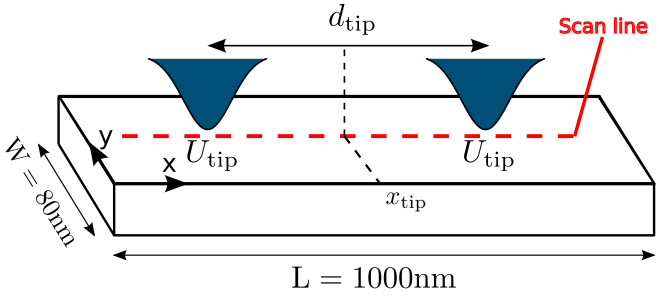

FIG. 1. (Color online) Sketch of the system considered in Secs. III and IV. We consider a channel of width $W = 80$ nm and the system of two tips with the same amplitude $U_{\text{tip}} = 5$ meV and width $w_{\text{tip}} = 15$ nm. The length of the computational channel is $L = 1000$ nm. The tips are above the axis of the channel (red dashed line) and are separated by a distance d_{tip}. The center of the system of two tips is located at position x_{tip}.

III. IMPURITIES MAPPING

Let us start our discussion with the device presented in Fig. 1. We consider a long (1000 nm) and narrow (80 nm) channel. For the Fermi energy $E_F = 2.5$ meV, there is only one current-propagating transverse mode in the channel ($M = 1$). We consider a double-tip system assuming that tips move along the x axis. The center of the system of the two tips is denoted by x_{tip} (see Fig. 1). Both tips are separated by a distance of d_{tip}. We assume $U_{\text{tip}} = 5$ meV and $w_{\text{tip}} = 15$ nm, For a *single* tip with these parameters, the conductance of the system is reduced to $G = 0.12G_0$. In Fig. 2(a), we show the result for the conductance G of the system as a function of x_{tip} and the intertip distance d_{tip} for a clean channel. The d_{tip} dependence of conductance reveals a series of resonances, separated by a distance $\lambda_F/2 \approx 60$ nm, which are related to the formation of the Fabry-Pérot interferometer [4,8] between the two tips. The interferometer induced by the two tips can probe the Fermi wavelength.

Let us now consider the system with a single potential defect present in the middle of the channel. The defect is modeled with Eq. (2) with $U_{\text{imp}} = 2$ meV and $w_{\text{imp}} = 10$ nm [see the potential profile below Fig. 2(b)]. Now the SGM image reveals new features, i.e., the resonance lines bend

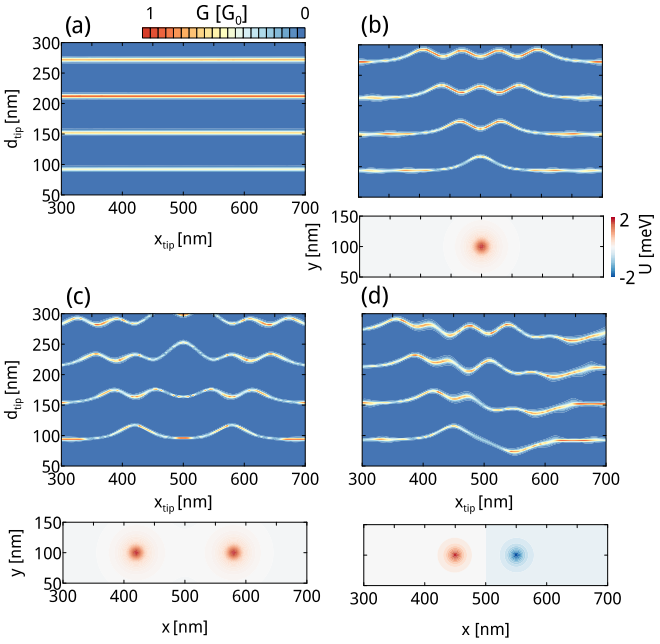

FIG. 2. (Color online) Results for $E_F = 2.5$ meV (one band transport). (a) The DT scan obtained for a clean channel. (b) Added impurity in the middle of the channel with amplitude $U_{imp} = 2$ meV and of width $w_{imp} = 10$ nm modeled with Eq. (2). (c) The same as (b) but for two impurities separated by distance 160 nm, and (d) obtained for two impurities of different sign ± 2 meV separated by distance 100 nm. The plots below show the potential profile in the channel for each case [(b)–(d)].

and oscillate in the vicinity of the impurity. Far from the impurity, the resonance lines return to the same position as in Fig. 2(a). Note that the first resonance line (around $d_{tip} \approx$ 90 nm) resembles the potential profile inside the channel. In Figs. 2(c) and 2(d), we show that the first resonance line follows the potential profile of the defect. This effect can be explained in terms of the semiclassical WKB approximation. For slowly varying potential $U(x)$ and $E_F > U(x)$, the wave vector of the propagating wave function $e^{\pm ik_F x}$ is given by $k_F = \sqrt{2m_{eff}[E_F - U(x)]}/\hbar$. Now if $U(x) > 0$, the phase of the wave propagating through the potential hill will be delayed by some value $\Delta\psi$ in comparison to the phase of the unperturbed system. Thus in order to restore the resonance for a standing wave, one must increase the distance between the tips by a value that compensates for the delayed $\Delta\psi$ phase. For $U(x) < 0$, the distance between the DT has to be decreased [see Fig. 2(d)]. Note that the proposed detection scheme resolves only the average Fermi wavelength and their shifts along the channel. One can detect the presence, position, and a character of the potential defect (repulsive or attractive), but not the quantitative potential profile of the defect.

In Fig. 3 we show the results for the channel with two impurities [same as in Fig. 2(c)] but for higher energies E_F. The results of Figs. 3(a) and 3(b) correspond to $M = 2$, although for $E_F = 7.5$ meV the threshold for $M = 3$ is only slightly higher in energy. At higher energies [Fig. 3(a)], the resolution of the images is reduced with the resonance lines getting closer and wider, but the image still allows one to map the defect potential distribution along the channel. Note that in Fig. 3(a),

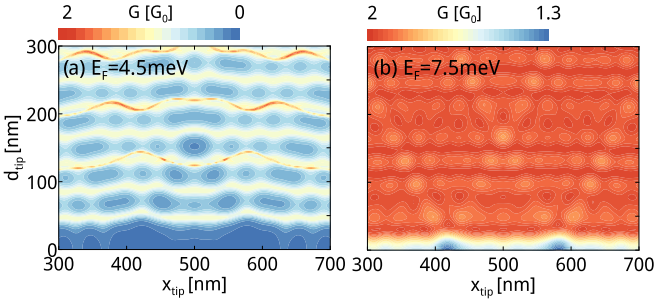

FIG. 3. (Color online) The same as in Fig. 2(c) but for higher Fermi energies. (a) Results for $E_F = 4.5$ meV (two band transport) and (b) $E_F = 7.5$ meV.

we notice the resonances of Fig. 2(c) for both the lowest subband (resonance sequence starting near $d_{tip} \simeq 30$ nm) and the second transverse mode (the sequence starts for $d_{tip} \simeq$ 100 nm). Note that the resonances corresponding to the second transverse subband are distinctly thinner—in this subband, the kinetic energy of motion along the channel (or simply the wave vector) is small, so the lifetime of the resonances trapped within the interferometer is larger. The states of the second subband possess a nodal line at the axis of the channel, and the results of Fig. 3(a) were gathered for the tips at this axis. The distinct conductance response of the second subband occurs since the width of the tip is large compared to the width of the channel, $2w_{tip}/W \simeq 0.4$. For $E_F = 7.5$ meV [see Fig. 3(b)], the image loses the features visible in Fig. 2, but the W-shaped line clearly indicates the position of the defects.

For completeness, we considered a clean channel with the width of the tip potential increased to $w_{tip} = 50$ nm. In Fig. 4 we plotted the conductance as a function of the intertip distance d_{tip} and the height of the tip potential. For $U_{tip} = 2$ meV, the system is transparent for the electron flow, and the formation of the resonances, as discussed above for $w_{tip} = 15$ nm, appears higher in energy. For $U_{tip} > 3.5$ meV, the ballistic electron flow is blocked. For larger values of U_{tip}, the formation of a

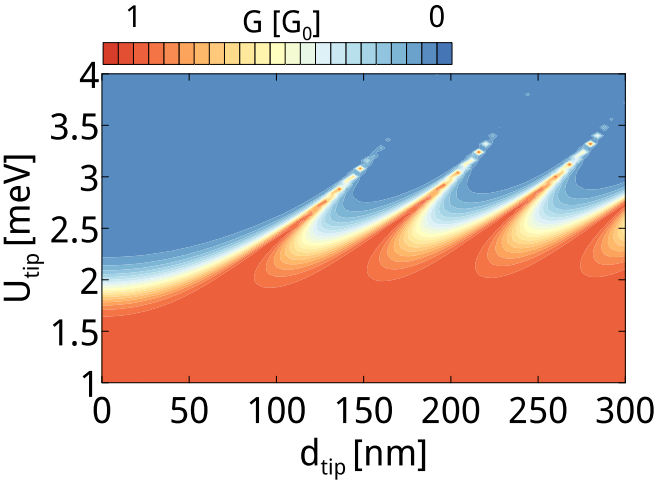

FIG. 4. (Color online) Conductance of the system as a function of the tip amplitude U_{tip} and distance d_{tip} between the tips obtained for $E_F = 2.5$ meV and width of the tip potential $w_{tip} = 50$ nm.

quantum dot supported by the tips should be expected with the transport dominated by the Coulomb blockade, which is, however, beyond the scope of the present work. The best resolution of the scan as a function of d_{tip} is obtained just below the cutoff of the ballistic transport.

To conclude this section, we find that the double-tip system can be used to read out the Fermi wavelength and the potential profile along the channel.

IV. TRANSVERSE MODE FILTER

In Fig. 3(a) we observed the resonances of the first and second subband (the red lines near $d_{tip} = 100$, 200, and 300 nm). These resonances occur separately or in overlap with the lines of the lowest resonance, depending on the values of d_{tip} and x_{tip}. Thus choosing a proper value of d_{tip} and x_{tip}, one can make a device that will filter out specific modes. For the proof of principle, we will restrict our consideration to the first and second mode. The resonance lines are plotted in Fig. 5(a) as functions of the distance between the tips and the Fermi energy for the clean channel (as in Fig. 1) but with the width increased to $W = 100$ nm. At low Fermi energies, only the first transverse mode is present in the conductance, and the double tip stops the transport unless the Fermi energy coincides with the resonances localized between the tips. For higher values of E_F, the resonance lines of the second mode appear in the (d_{tip},E_F) plane and intersect with the first mode lines. Figures 5(b)–5(f) show the electron density for work points marked by arrows in Fig. 5(a). We can see that for a given energy E_F, one may filter out a specific transverse mode by changing the d_{tip} distance. Upon filtering, one can select low-energy modes and block high energy, or vice versa. The mode filtering should be visible in the angular branching of the

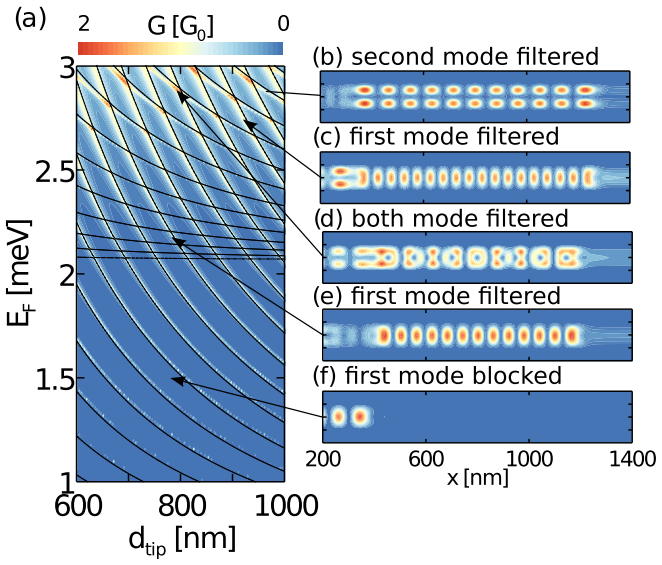

FIG. 5. (Color online) (a) The conductance G of the long channel of width $W = 100$ nm as a function of d_{tip} and E_F. Dashed lines in (a) show the energy spectrum of a two-dimensional quantum well of length $d_{tip} - 2w_{tip}$. The shift by $2w_{tip}$ accounts for the finite size of the tip potential. (b)–(f) Electron density $|\psi|^2$ obtained for values of (d_{tip},E_F) indicated by arrows.

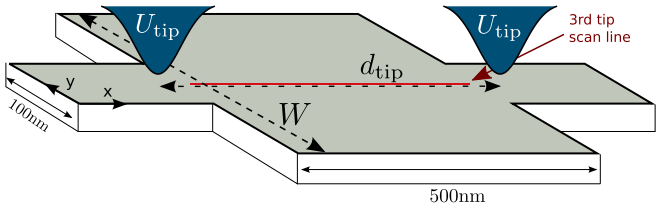

FIG. 6. (Color online) Sketch of the second system considered in this paper. A long channel of width 100 nm is coupled to the resonant cavity of variable width W and length 500 nm. As before, we have two tips in the system: one in the left lead and the second in the right lead. Both tips have the same parameters of $U_{tip} = 5$ meV and $w_{tip} = 15$ nm and are separated by a distance d_{tip}. The red line corresponds to the third tip scan discussed in Sec. VI.

current flow in the SGM of quantum point contacts [4]. Also, the SGM readout of the double-slit interference [27] should be simplest for a single incident subband, since the contributions of various modes cancel in the Landauer summation [27]. The mode filtering can be used/tested against the Young interference features in the SGM images.

In Fig. 5(a) we plotted the energy spectrum of a quantum well of width 100 nm, length $d_{tip} - 2w_{tip}$, and infinite potential profile. The conductance resonances follow the energy spectrum exactly for an infinite quantum well.

V. DETECTION OF LOCALIZED RESONANCES

Let us now consider the system depicted in Fig. 6 with a channel of width 100 nm connected to the quantum cavity of length 500 nm and width W. To get the best resolved images, we set $E_F = 2$ meV (single subband transport within the channel). In Fig. 7(a) we show the conductance of the system as a function of the d_{tip} and width W of the cavity. We kept the center of the double tip fixed in the middle of the

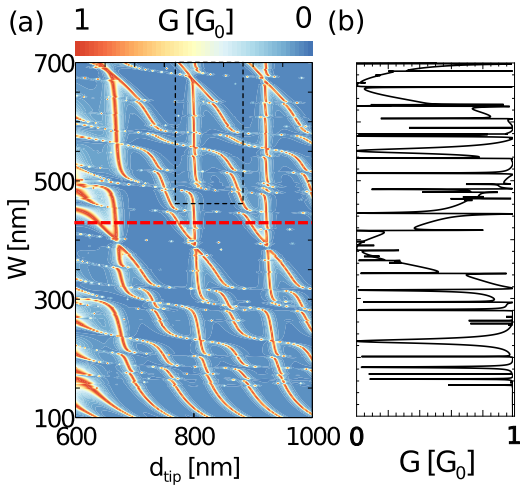

FIG. 7. (Color online) (a) The conductance of the system depicted in Fig. 6 as a function of d_{tip} and cavity width W. The dashed rectangle corresponds to the zoomed area shown in Fig. 8(a). The red line corresponds to the scan with the third tip discussed in the next paragraph. (b) Conductance of the system presented in Fig. 6 as a function of W but without DT.

resonant cavity. For small values of W around 100 nm, the resonance lines are very similar to those of Fig. 5(a). For a changed width of the cavity, the cavity-localized energy levels vary as $\propto W^{-2}$. Thus changing the width W, we should expect the behavior of the resonance lines to be similar to those of Fig. 5(a). Large values of W lead to a complex behavior of the resonance lines but with well-distinguishable patterns of X-shaped lines, which appear with a period of λ_F along the d_{tip} axis.

In Fig. 7(b) we show the conductance of the system without the tips. The conductance contains a series of sharp resonances of a Fano type corresponding to quasibound states localized within the cavity. Most of the resonances visible in Fig. 7(b) are also present in Fig. 7(a) as nearly horizontal lines—independent of the distance between the tips—which suggests that they correspond to the quasilocalized stated of the cavity. The nearly horizontal lines are very thin, indicating a long lifetime of the resonances. The lines with a steeper dependence on d_{tip} in Fig. 7(a) correspond to resonances supported by the tips. The lines are wide, indicating a stronger coupling to the channel. A study probing the conductance as a function of the distance between the tips would be an experimental implementation of the stabilization methods [28] for detection of localized resonances.

The zoomed region of Fig. 7 marked by a black rectangle is depicted in Fig. 8(a). In this picture, we can distinguish three types of resonance lines: (a) vertical, almost independent of the width W of the cavity; (b) resonances, which vary with W; and (c) well-visible horizontal resonances, independent of the distance between DT, which correspond to the quasilocalized state in the cavity. We found in general that the difference between the two first types of resonances comes from the symmetry of the resonant scattering densities. The scattering densities for lines of type (a) and (b) are symmetric with respect to the center of the cavity in the x direction. The resonances that are independent of W have a nodal surface at the symmetry axis, while the other have a maximum on the symmetry line. The former are strongly localized in the center of the cavity [see Figs. 8(b)–8(d)] and the latter form resonances that are delocalized over the entire cavity [see Figs. 8(f), (g), and (i)]. The delocalized resonances react stronger to the value of W in Fig. 7(a). Figure 8(h) shows a resonance of a third type—of energy that is weakly dependent on d_{tip}—that corresponds to the resonances supported by the cavity itself. Note that outside the resonance lines, the asymmetry of the electron injection is translated to asymmetry of the scattering density [see Fig. 8(e)]. For resonances, the incidence direction cannot be extracted from the scattering density [Figs. 8(b)–8(d) and 8(f)–8(i)].

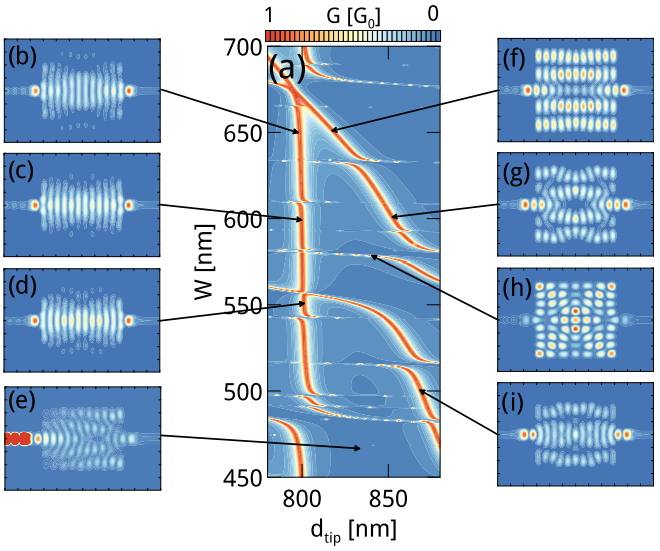

FIG. 8. (Color online) (a) Zoom of Fig. 7(a) marked by a dashed rectangle. (b)–(i) Probability density for the the electron incoming from the left for d_{tip} and W pointed by the arrows. (b)–(d) Antisymmetric resonances, (e) an off-resonant scattering probability density, and (f)–(i) symmetric resonances.

In experiments, variation of the geometry of the cavity can be accomplished by tuning an electrostatic confinement in the y direction due to external gating. Since the electrostatic confinement potential is usually parabolic at its origin, we replaced the hard-wall confinement by

$$U_{\text{parabolic}} = \tfrac{1}{2}\omega'^2 y^2 = \tfrac{1}{2}(3\ \text{meV} - \omega)^2 y^2. \tag{5}$$

With this potential, the effective width of the cavity is controlled by the harmonic-oscillator energy. The parametrization was chosen in order to get a better comparison with Fig. 7. The value $\omega = 3$ meV $\Rightarrow \omega' = 0$ meV corresponds to a small value of W in Fig. 6 and channel-like behavior of conductance. The value $\omega = 0$ meV $\Rightarrow \omega' = 3$ meV corresponds to the large values of W. Comparing Figs. 7 and 9, we can see that

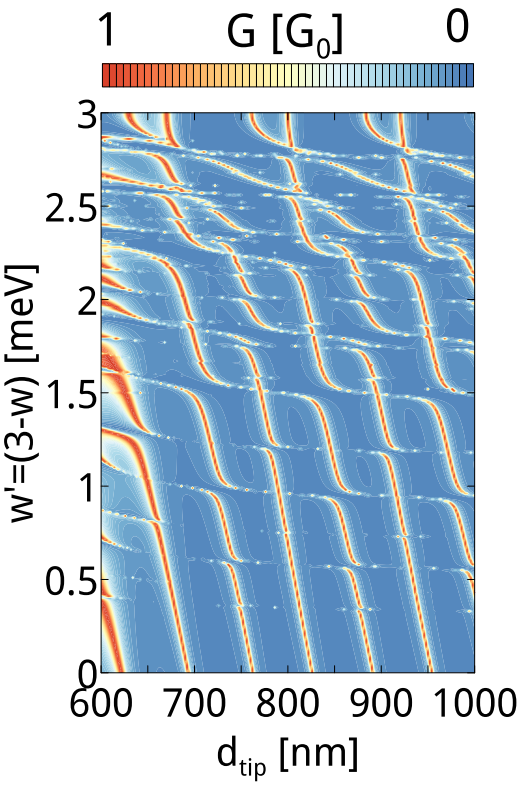

FIG. 9. (Color online) The conductance of the system depicted in Fig. 6 as a function of d_{tip} and angular frequency ω of the oscillator. The parametrization $\omega' = 3$ meV $- \omega$ is applied in order to keep the same interpretation of the y axis (width of the cavity) as in Fig. 7(a).

both share the same features: (a) X-shaped resonance lines are present, (b) some resonances depend weakly on W as a function of the cavity width (antisymmetric ones) and some vary with $d_{\rm tip}$ (symmetric states), and (c) horizontal resonance lines are also present. Note that for a smooth potential, we find in the conductance image resonances of a large slope (Fig. 9) but which are not strictly vertical as for the cavity with the rectangular confinement potential (cf. Figs. 7 and 8). This is because the variation of ω changes the potential profile in the whole cavity and not only the width of the cavity (as it was in the previous example). Note that according to the above discussion, the slope of the vertical resonance lines should provide information on the shape of the confinement potential within the cavity.

Concluding this section, we found that using a double-tip system with a cavity of variable width, one may tune the system to a specific resonance: (i) symmetric or antisymmetric resonances supported between the tips, or (ii) resonances quasilocalized within the cavity (horizontal lines in Figs. 7 and 9).

VI. MAPPING THE LOCAL DENSITY AT THE FERMI LEVEL

Let us now discuss the possibility of mapping the LDOS inside the potential cavity presented in Fig. 6. Our recent modeling [2,29] indicated that for a cavity strongly coupled to the channel, the LDOS can only be extracted from the (single-tip) conductance maps provided that the Fermi energy coincides with the energy of localized resonances. Only in the conditions of the Fano resonance is the conductance map strongly correlated with LDOS. In III–V nanostructures, the variation of the Fermi energy is far from straightforward. However, with the two tips moving inside the channels (Fig. 6), one can induce the resonant conditions without the need to change the Fermi energy, and then scan for the local density of states using a third tip.

In general, the conductance maps are highly correlated to the local density of states when the electron scattering wave functions incoming from the left and right leads are the same up to a constant phase. The latter case can be supported [29] by the perturbation theory [30,31] for which the first-order correction to the conductance is simply proportional to LDOS. The scattering densities for the electron incoming from the left lead plotted for resonant conditions induced by the two tips [Figs. 8(b)–8(d) and 8(f)–8(i)] are highly symmetric: nearly identical densities are obtained for the electrons incident from the right. Thus for the inverted current direction, the scattering density inside the cavity stays the same, and this should lead to good correlation between LDOS and the corresponding G map [29]. Conversely, in off-resonant conditions [cf. Fig. 8(e)], the scattering density is asymmetric with respect to the channels, and the correlation between LDOS and G can be expected to be low.

We consider a cavity of Fig. 7(a) with $W = 430$ nm. The assumed third-tip parameters are $U_{\rm tip} = 1$ meV and $w_{\rm tip} = 10$ nm. We need a pronounced variation of G as a function of the tip position, and the adopted height of the tip potential is quite large as compared to the Fermi energy kept at 2 meV.

Figure 10(a) shows the conductance of the system depicted in Fig. 6 as a function of distance between the two tips inside the channels, $d_{\rm tip}$ (see Fig. 7), and the position of the third tip, $x_{\rm tip}$, along the axis of the system (red line in Fig. 6). We observe a number of resonances for a sequence of $d_{\rm tip}$. The $d_{\rm tip}$ distance, which corresponds to resonances, can also be

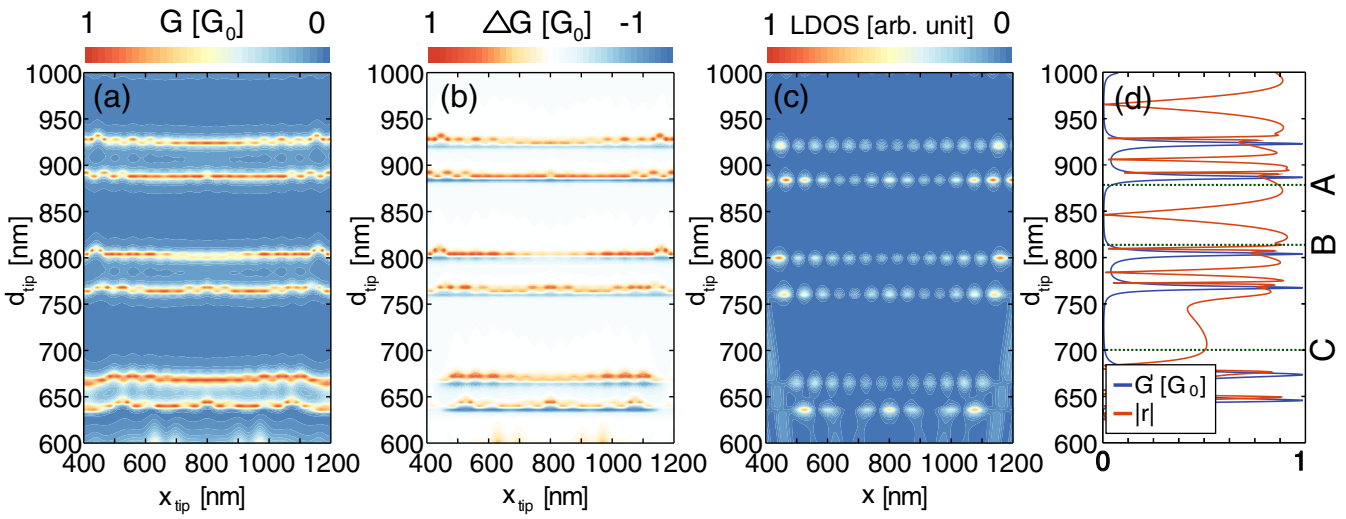

FIG. 10. (Color online) (a) Conductance G of the cavity [parameters corresponding to the red line in Fig. 7(a)] as a function of the third-tip position, $x_{\rm tip}$, moved along the axis of the system marked by the red line in Fig. 6, and the distance between the two tips, $d_{\rm tip}$, that stay within the channel. (b) $\Delta G = G - G'$ as functions of $x_{\rm tip}$ and $d_{\rm tip}$, where G' is the conductance of the system without the third tip. (c) Local density of states in the absence of the third tip along the axis of the system—line of the scan used in (a) and (b). For evaluation of the LDOS, we normalized the scattering densities to the unity within the computational box. For off-resonant conditions, where the scattering density is large only inside the channels [cf. Fig. 8(e)], we obtain a strong reduction of LDOS within the cavity—see Fig. 10(c). (d) Conductance G' of the system as a function of $d_{\rm tip}$ without the third tip (blue line). Absolute value of Pearson correlation r between (a) and (c) images calculated from Eq. (6) (red line).

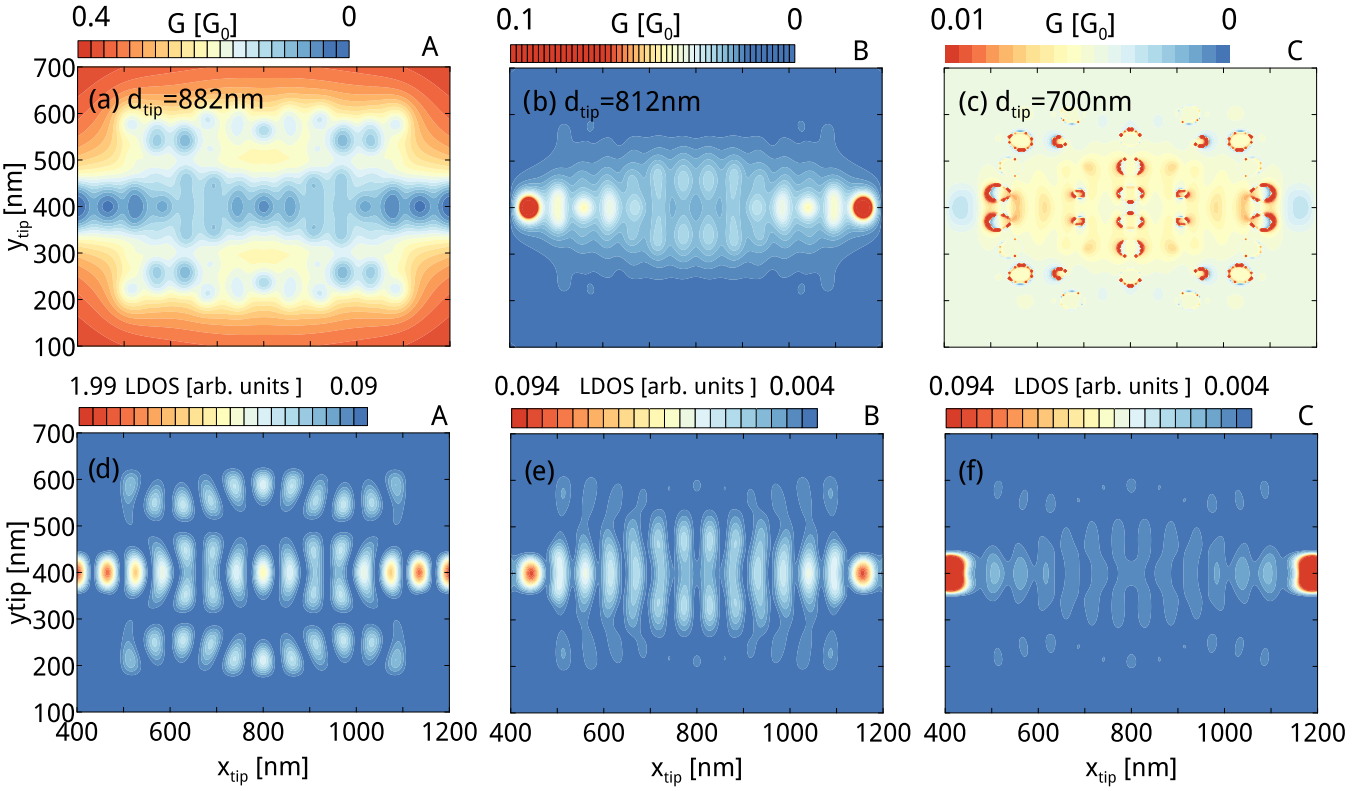

FIG. 11. (Color online) (a)–(c) The SGM image and (d)–(f) the LDOS obtained for points A, B, and C in Fig. 10(d). Point A corresponds to the symmetric resonance induced by the double-tip system in the work point where the correlation r is negative. Point B corresponds to the antisymmetric resonance with positive correlation r. Point C corresponds to a zero of T in the absence of the tip.

deduced from the $G(d_{\rm tip})$ dependence of the cavity–double-tip system (without the third tip), which is plotted in Fig. 10(d).

In Fig. 10(b) we present the conductance change $\Delta G = G(x_{\rm tip},d_{\rm tip}) - G'(d_{\rm tip})$ induced by the third tip with respect to conductance G' of the system without the third tip. Note that ΔG changes sign in the vicinity of the resonance induced by the double tip [see the blue curve in Fig. 10(d) for the location of the resonances]. To compare the conductance obtained from a scan with the third tip, $G_{\rm scan} \equiv G(x_{\rm tip},d_{\rm tip})$, with the obtained LDOS on that line, $L_{\rm scan} = {\rm LDOS}(x_{\rm tip},d_{\rm tip})$ (for a given value of $d_{\rm tip}$), we calculate the Pearson correlation $r \equiv r(d_{\rm tip})$,

$$r = \frac{\int (G_{\rm scan} - \langle G_{\rm scan}\rangle)(L_{\rm scan} - \langle L_{\rm scan}\rangle) dx_{\rm tip}}{\Delta_L \sigma(G_{\rm scan})\sigma(L_{\rm scan})}, \qquad (6)$$

where $\langle a\rangle = \frac{1}{\Delta_L}\int a(x_{\rm tip})dx_{\rm tip}$ is the average value of a, $\sigma^2(a) = \frac{1}{\Delta_L}\int [a(x_{\rm tip}) - \langle a\rangle]^2 dx_{\rm tip}$ is the standard deviation of a, and $\Delta_L = 800$ nm is the length of the scan along the red line in Fig. 6. Before the calculation of r, both functions $G_{\rm scan}$ and $L_{\rm scan}$ were normalized to range from 0 to 1. The absolute value of the correlation r is plotted in Fig. 10(d) with the red line. Note that r increases to about 0.9 near the induced resonances, which means that the obtained G maps well-resolve the LDOS inside the cavity—see the points marked by A or B in the figure. Outside the resonances (point C, for instance), the correlation is much lower. In the figure, the abrupt dips in the $r(d_{\rm tip})$ dependence result from the fact that the correlation coefficient changes sign at the resonances [29].

In Fig. 11 we present the SGM images and corresponding LDOS for points A, B [Fig. 10(d)]—near the resonances induced by the two tips in the channels, and for point C—outside a resonance (for $G \simeq 0$ in fact). A close correspondence between LDOS and G is reached in the resonant points A and B with no evident correspondence in off-resonant point C.

Summarizing, the usage of multiple tips allows for (i) tuning the system to a resonance and then (ii) an accurate readout of the local density of states.

VII. TIP AS A PART OF THE SCATTERING SYSTEM

The scanning gate microscope tip can be used as a part of the scattering system, with the other tip gathering the conductance maps. In particular, the tip potential placed near the exit of the quantum point contact has been used to form a quantum Hall interferometer [32]. A similar quantum Hall system including a potential defect spontaneously formed at the exit from the QPC constriction was studied with scanning gate microscopy in Ref. [33].

The SGM with a double-tip system can be used for observation of the Young interference [27] for a setup depicted in Fig. 12. The SGM signal was predicted [27] to contain signatures of the double-slit interference for low-energy transport. The proposed [27] setup requires a beam splitter—a central obstacle for electron flow, which may be difficult to introduce in the form of a fixed gate. A floating one—introduced by the

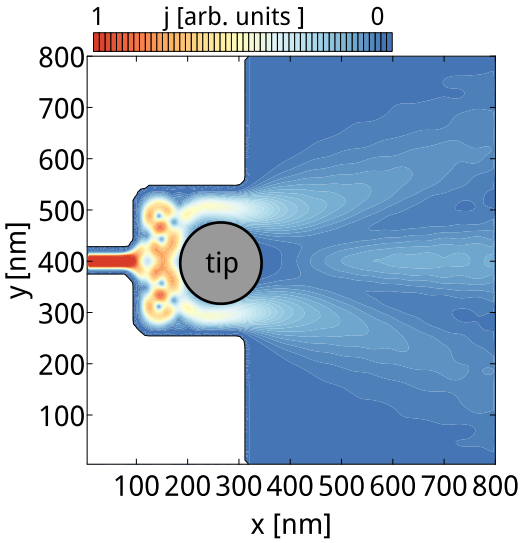

FIG. 12. (Color online) Schematics of the system with a quantum point contact and the tip potential for observation of the Young interference and the calculated scattering density current $|j(x,y)|$ including the double-slit interference pattern. The applied tip potential parameters are $w_{\text{tip}} = 50$ nm and $U_{\text{tip}} = 10$ meV.

tip—is a possible option. In Fig. 12 we plotted a system with the QPC slit entering a small open cavity. The potential of the tip (schematically shown with the gray circle) was introduced near the exit of the cavity to an unconfined half-plane. The scattering density current $|j(x,y)|$ plot in Fig. 12 shows the formation of the interference pattern characteristic of Young interference [27]. The other tip used as an electron flow detector could then be used for readout of the double-slit interference in the SGM conductance images.

VIII. CONCLUSIONS

We have studied numerically the possible applications of the multitip scanning gate microscopy on the systems with 2DEG. We found that the measurements using a pair of tips allow for (i) readout of the Fermi wavelength, (ii) detection of the potential defects with an indication of their position and attractive/repulsive character, (iii) filtering of specific transverse modes, and (iv) tuning the system into a resonance that allows for a reliable detection of the local density of states with a third tip.

ACKNOWLEDGMENTS

This work was supported by the National Science Centre according to the decision DEC-2012/05/B/ST3/03290, and by PL-Grid Infrastructure. K.K. is supported by the scholarship of the Krakow Smoluchowski Scientific Consortium from the funding for the National Leading Research Centre by the Ministry of Science and Higher Education (Poland). B.H. is a research associate of the FRS-FNRS. This work is also supported by FRS-FNRS Projects No. J.0067.13 and No. U.N025.14, and by the ARC Project No. 11/16-037.

[1] H. Sellier, B. Hackens, M. G. Pala, F. Martins, S. Baltazar, X. Wallart, L. Desplanque, V. Bayot, and S. Huant, Semicond. Sci. Technol. **26**, 064008 (2011); D. K. Ferry, A. M. Burke, R. Akis, R. Brunner, T. E. Day, R. Meisels, F. Kuchar, J. P. Bird, and B. R. Bennett, *ibid.* **26**, 043001 (2011).

[2] K. Kolasiński and B. Szafran, Phys. Rev. B **88**, 165306 (2013).

[3] K. E. Aidala, R. E. Parrott, T. Kramer, E. J. Heller, R. M. Westervelt, M. P. Hanson, and A. C. Gossard, Nature Physics **3**, 464 (2007).

[4] M. A. Topinka, B. J. LeRoy, S. E. J. Shaw, E. J. Heller, R. M. Westervelt, K. D. Maranowski, and A. C. Gossard, Science **289**, 2323 (2000).

[5] M. A. Topinka, B. J. LeRoy, R. M. Westervelt, S. E. J. Shaw, R. Fleischmann, E. J. Heller, K. D. Maranowski, and A. C. Gossard, Nature (London) **410**, 183 (2001).

[6] M. G. Pala, S. Baltazar, P. Liu *et al.*, Phys. Rev. Lett. **108**, 076802 (2012); A. A. Sousa, A. Chaves, G. A. Farias, and F. M. Peeters, Phys. Rev. B **88**, 245417 (2013); M. D. Petrovic, F. M. Peeters, A. Chaves, and G. A. Farias, J. Phys.: Condens. Matter **25**, 495301 (2013).

[7] A. A. Kozikov, R. Steinacher, C. Roessler *et al.*, New J. Phys. **16**, 053031 (2014).

[8] M. P. Jura, M. A. Topinka, M. Grobis, L. N. Pfeiffer, K. W. West, and D. Goldhaber-Gordon, Phys. Rev. B **80**, 041303(R) (2009).

[9] B. Hackens, F. Martins, S. Faniel *et al.*, Nat. Commun. **1**, 39 (2010).

[10] H. Sellier, B. Hackens, M. G. Pala *et al.*, Semicond. Sci. Technol. **26**, 6 (2011); F. Martins, B. Hackens, M. G. Pala *et al.*, Phys. Rev. Lett. **99**, 136807 (2007).

[11] M. G. Pala, B. Hackens, F. Martins, H. Sellier, V. Bayot, S. Huant, and T. Ouisse, Phys. Rev. B **77**, 125310 (2008).

[12] P. Fallahi, A. C. Bleszynski, R. M. Westervelt, J. Huang, J. D. Walls, E. J. Heller, M. Hanson, and A. C. Gossard, Nano Lett. **5**, 223 (2005); A. Pioda, S. Kièin, T. Ihn, M. Sigrist, A. Fuhrer, K. Ensslin, A. Weichselbaum, S. E. Ulloa, M. Reinwald, and W. Wegscheider, Phys. Rev. Lett. **93**, 216801 (2004); A. C. Bleszynski-Jayich, L. E. Fröberg, M. T. Björk, H. J. Trodahl, L. Samuelson, and R. M. Westervelt, Phys. Rev. B **77**, 245327 (2008); L. M. Zhang and M. M. Fogler, Nano Lett. **6**, 2206 (2006); J. Qian, B. I. Halperin, and E. J. Heller, Phys. Rev. B **81**, 125323 (2010).

[13] M. Ishikawa, M. Yoshimura, and K. Ueda, J. Appl. Phys. **44**, 1502 (2005).

[14] S. Yoshimoto, Y. Murata, K. Kubo, K. Tomita, K. Motoyoshi, T. Kimura, H. Okino, R. Hobara, I. Matsuda, S. Honda, M. Katayama, and S. Hasegawa, Nano Lett. **7**, 956 (2007).

[15] T. H. Kim, X.-G. Zhang, D. M. Nicholson, B. M. Evans, N. S. Kulkarni, B. Radhakrishnan, E. A. Kenik, and A.-P. Li, Nano Lett. **10**, 3096 (2010).

[16] C. Durant, M. Berthe, Y. Makoudi, J.-P. Nys, R. Leturcq, P. Caroff, and B. Grandidier, Nanotechnology **24**, 275706 (2013).

[17] A. E. Gildemeister, T. Ihn, M. Sigrist, K. Ensslin, D. C. Driscoll, and A. C. Gossard, Phys. Rev. B **75**, 195338 (2007); R. Steinacher, A. A. Kozikov, C. Rössler, C. Reichl, W. Wegscheider, T. Ihn, and K. Ensslin, New J. Phys. **17**, 043043 (2015).
[18] B. Szafran, Phys. Rev. B **84**, 075336 (2011).
[19] R. Crook, C. G. Smith, M. Y. Simmons, and D. A. Ritchie, Phys. Rev. B **62**, 5174 (2000).
[20] E. E. Boyd and R. M. Westervelt, Phys. Rev. B **84**, 205308 (2011).
[21] D. J. Kirkner and C. S. Lent, J. Appl. Phys. **67**, 6353 (1990).
[22] M. Leng and C. S. Lent, J. Appl. Phys. **76**, 2240 (1994).
[23] K. Kolasinski and B. Szafran, Phys. Rev. B **89**, 165306 (2014).
[24] M. Zwierzycki, P. A. Khomyakov, A. A. Stariko K. Xia, M. Talanana, P. X. Xu, V. M. Karpan, I. Marushchenko, I. Turek, G. E. W. Bauer, G. Brocks, and P. J. Kelly, Phys. Status Solidi B **245**, 623 (2008).
[25] C. W. Groth, M. Wimmer, A. R. Akhmerov, and X. Waintal, New J. Phys. **16**, 063065 (2014).
[26] J. W. Demmel, S. C. Eisenstat, J. R. Gilbert, X. S. Li, and J. W. H. Liu, SIAM. J. Matrix Anal. Appl. **20**, 720 (1999).
[27] K. Kolasinski, B. Szafran, and M. P. Nowak, Phys. Rev. B **90**, 165303 (2014).
[28] V. A. Mandelshtam, T. R. Ravuri, and H. S. Taylor, Phys. Rev. Lett. **70**, 1932 (1993).
[29] K. Kolasinski and B. Szafran, New J. Phys. **16**, 053044 (2014).
[30] R. A. Jalabert, W. Szewc, S. Tomsovic, and D. Weinmann, Phys. Rev. Lett. **105**, 166802 (2010).
[31] C. Gorini, R. A. Jalabert, W. Szewc, S. Tomsovic, and D. Weinmann, Phys. Rev. B **88**, 035406 (2013).
[32] N. Pascher, F. Timpu, C. Rössler, T. Ihn, K. Ensslin, C. Reichl, and W. Wegscheider, Phys. Rev. B **89**, 245408 (2014).
[33] F. Martins, S. Faniel, B. Rosenow, M. G. Pala, H. Sellier, S. Huant, L. Desplanque, X. Wallart, V. Bayot, and B. Hackens, New J. Phys. **15**, 013049 (2013).